

# Horizontal shear instabilities in rotating stellar radiation zones

## I. Inflectional and inertial instabilities and the effects of thermal diffusion

J. Park, V. Prat and S. Mathis

AIM, CEA, CNRS, Université Paris-Saclay, Université Paris Diderot, Sorbonne Paris Cité, F-91191 Gif-sur-Yvette, France  
e-mail: junho.park@cea.fr

### ABSTRACT

**Context.** The so-called rotational mixing, which transports angular momentum and chemical elements in stellar radiative zones, is one of the key processes for modern stellar evolution. In the two last decades, the stress has been put on the turbulent transport induced by the vertical shear instability. However, the instabilities of horizontal shears and the strength of the anisotropic turbulent transport they may trigger are still largely unknown. This is the weakest point of the current theory of the hydrodynamical rotational mixing in which we assume an anisotropic turbulent transport stronger along the horizontal directions than along the vertical one.

**Aims.** This paper investigates for the first time the combined effects of stable stratification, rotation, and thermal diffusion on the instabilities of horizontal shears. The obtained general results are discussed in the context of stellar radiative zones.

**Methods.** The eigenvalue problem describing the linear instabilities of a flow with a hyperbolic-tangent horizontal shear profile is solved numerically for a wide range of parameters. Furthermore, the Wentzel-Kramers-Brillouin-Jeffreys (WKBJ) approximation is applied when this is possible to provide explicit asymptotic dispersion relations in non-diffusive and highly diffusive limits. As a first step, we consider a polar  $f$ -plane where the gravity and the rotation vector are aligned.

**Results.** Two types of instabilities are identified: the inflectional and the inertial instabilities. The inflectional instability, which is related to the second-derivative of the shear, is most unstable at finite streamwise wavenumber and zero vertical wavenumber, independently of the stratification, rotation, and thermal diffusion. It is favoured by stable stratification but stabilised by thermal diffusion. The rotation shifts it to small vertical wavenumbers and thus to largest scales. The inertial instability is driven by rotation; a largest angular velocity sustains a stronger instability. The WKBJ analysis reveals that its growth rate reaches its maximum  $\sqrt{f(1-f)}$  (where  $f$  is the dimensionless Coriolis parameter that corresponds to the inverse of the Rossby number) in the inviscid limit as the vertical wavenumber goes to infinity. The inertial instability for finite vertical wavenumber is stabilized as the stratification increases for non-diffusive fluids, while it becomes independent of the stratification and stronger for fluids with high thermal diffusivity. Parametric numerical study also confirms this independence of the stratification for both the inflectional and inertial instabilities for high thermal diffusivity. Furthermore, we found a self-similarity of the instabilities based on the rescaled parameter  $PeN^2$  with the Péclet number  $Pe$  and the Brunt-Väisälä frequency  $N$ .

**Key words.** hydrodynamics – turbulence – stars: rotation – stars: evolution

### 1. Introduction

The combination of space-based helio- and asteroseismology has demonstrated that stably stratified rotating stellar radiation zones are the seats of an efficient transport of angular momentum all along the evolution of stars. This strong transport leads to a uniform rotation in the case of the Sun down to  $0.2R_{\odot}$  (García et al. 2007) and to weak differential rotation in other stars (e.g. Mosser et al. 2012; Deheuvels et al. 2012, 2014; Kurtz et al. 2014; Saio et al. 2015; Murphy et al. 2016; Spada et al. 2016; Van Reeth et al. 2016; Aerts et al. 2017; Van Reeth et al. 2018; Gehan et al. 2018; Ouazzani et al. 2019). Four main mechanisms that transport angular momentum and mix chemicals are present in stellar radiation zones (e.g. Maeder 2009; Mathis 2013; Aerts et al. 2019, and references therein): instabilities of the differential rotation (e.g. Zahn 1983, 1992), stable and unstable magnetic fields (e.g. Spruit 1999; Fuller et al. 2019), internal gravity waves (e.g. Zahn et al. 1997; Talon & Charbonnel 2005; Pinçon et al. 2017), and large-scale meridional circulations (e.g. Zahn 1992; Maeder & Zahn 1998; Mathis & Zahn 2004). Important progresses have been achieved for their modelling during the last two decades. However, a lot of simplifying assumptions are still

assumed in their treatment because of their complexity and of the broad range of spatial and temporal scales they involve. For instance, the complex interplay between rotation and stratification for the study of vertical and horizontal shear instabilities is partially treated. On the one hand, the action of the Coriolis acceleration is not taken into account in the state-of-the-art modelling of the vertical turbulent transport due to the instabilities of a radial differential rotation. On the other hand, the important action of thermal diffusion has completely been ignored in the studies of the horizontal turbulent transport induced by vertical and horizontal shears instabilities (see e.g. Mathis et al. 2018, 2004, respectively). As a consequence, a lot of efforts are still needed to get robust ab-initio prescriptions for transport processes in stars and to reconcile stellar models and the observations (e.g. Eggenberger et al. 2012; Ceillier et al. 2013; Marques et al. 2013; Cantiello et al. 2014; Eggenberger et al. 2019). In this work, our aim is to improve our understanding of horizontal shear instabilities in rotating stellar radiation zones.

In his seminal article, Zahn (1992) built the theoretical framework to study the turbulent transport induced by vertical and horizontal shears in convectively stable rotating stellar radiation zones. In such regions, turbulence can be anisotropic be-

cause of the combined action of buoyancy and the Coriolis acceleration, which control the turbulent motions along the vertical and the horizontal directions, respectively (e.g. Billant & Chomaz 2001; Davidson 2013; Mathis et al. 2018). As pointed out in Mathis et al. (2018), many theoretical works have been devoted to provide robust prescriptions for the vertical eddy diffusion associated with the instability of vertical shears (e.g. Zahn 1992; Maeder 1995; Maeder & Meynet 1996; Maeder 1997; Talon & Zahn 1997; Kulenthirarajah & Garaud 2018). Their predictions are now tested using direct numerical simulations (Prat & Lignières 2013, 2014; Prat et al. 2016; Garaud et al. 2017; Gagnier & Garaud 2018). However, very few studies have examined the instabilities of horizontal shears (e.g. Zahn 1992; Maeder 2003; Mathis et al. 2004). The resulting prescriptions are based mostly on phenomenological approaches and results of experimental non-stratified Taylor-Couette set-up (Richard & Zahn 1999) that do not take into account the complex interplay of stratification, rotation, and thermal diffusion, which plays a key role in stellar radiation zones. For instance, heat diffusion inhibits the effects of the stable stratification for the vertical shear instability (Townsend 1958; Zahn 1983). Mathis et al. (2018) studied the combined action of stratification and rotation on the horizontal turbulent transport. But they have neglected the non-adiabatic aspects of the problem and they only focused on the latitudinal turbulent transport induced by the three-dimensional motions resulting from the instability of a vertical shear. This constitutes an important weak point of the theory for the rotational mixing, which has been successfully implemented in several stellar evolution codes (Talon et al. 1997; Meynet & Maeder 2000; Palacios et al. 2006; Marques et al. 2013). Indeed, in its formalism, a strongest turbulent transport is assumed along the horizontal direction than along the vertical. This allows us to assume that the horizontal gradients of the angular velocity (and of the fluctuations of temperature and chemical composition) are smoothed out leading to the so-called “shellular” rotation, which only varies with the radius. It is thus mandatory to study the instabilities of horizontal shears in rotating stably stratified stellar regions (Fig. 1a,b) with taking into account their important thermal diffusion.

In classical fluid dynamics, theories of shear flow stability in homogeneous fluids are well investigated (Schmid & Henningson 2001). According to Rayleigh’s inflection point criterion, an inviscid unstable shear flow should possess an inflectional point where the second derivative of the zonal flow velocity  $U$  vanishes (i.e.  $U''(y) = 0$ , where  $y$  is the local latitudinal coordinate; see Fig. 1c). For instance, a shear flow with a hyperbolic tangent velocity profile can undergo this inflection point instability (Michalke 1964). In geophysical fluid dynamics, this instability is also referred as the barotropic instability (Kundu & Cohen 2001) as it can be triggered by a two-dimensional horizontal perturbation with a finite streamwise zonal wavenumber  $k_x$ . However, general three-dimensional perturbations with both  $k_x$  and a vertical wavenumber  $k_z$  can also trigger the inflectional instability of the horizontal shear flow so we use the terminology inflectional instability hereafter. The stability analysis of such shear flow in stratified fluids by Deloncle et al. (2007) revealed that the unstable regime in the parameter space of zonal and vertical wavenumbers ( $k_x, k_z$ ) is widely broadened for a horizontal shear flow  $U(y)$  for strong stratification: perturbation with smaller vertical scale (i.e. large  $k_z$ ) can still be unstable in strongly stratified fluids with a large Brunt-Väisälä frequency  $N$ . A self-similarity of the three-dimensional inflectional instability is found for strong stratification with a rescaled parameter  $Nk_z$ . However, the most unstable perturbation is found

to be still two dimensional with a finite  $k_x$  at  $k_z = 0$  independent of the stratification.

Effects of both the stratification and rotation on horizontal shear instability are studied by Arobone & Sarkar (2012). They explored how the instability growth rate in the parameter space ( $k_x, k_z$ ) is modified as the stratification and rotation change. They found that the most unstable mode of the inflectional instability is always found at finite  $k_x$  and  $k_z = 0$  independent of the stratification and rotation. They also underlined that there exists an inertial instability in a finite range of  $f_0$  which is the Coriolis parameter defined as  $f_0 = 2\Omega \cos \theta_s$  where  $\Omega$  is the rotation of a star and  $\theta_s$  is the colatitude. The origin of the inertial instability is different from the inflectional instability: the horizontal flow can become inertially unstable only in rotating fluids if the Rayleigh discriminant  $\Phi(y) = f_0(f_0 - U')$  becomes negative (Fig. 1d). This condition leads to the inertially-unstable range  $0 < f_0 < \max(U')$  for the hyperbolic-tangent shear flow whose the maximum growth rate is found in inviscid limit as  $\sqrt{f_0(\max(U') - f_0)}$ . While these studies have investigated effects of the stratification and rotation on horizontal shear instabilities, it is still unknown how these instabilities are modified by the thermal diffusion which has an essential importance for the dynamics of stellar radiative zones.

In this paper, we investigate the linear stability of horizontal shear flows in stably-stratified, rotating and thermally-diffusive fluids in the context of stellar radiation zones. In Sect. 2, equations for the linear stability analysis are formulated. In Sect. 3, we compute numerical results of this analysis for both the inflectional and inertial instabilities to characterise their main properties. In Sect. 4, these results are compared with those from asymptotic analyses by means of the Wentzel-Kramers-Brillouin-Jeffreys (WKBJ) approximation for the inertial instability in order to understand the important role of thermal diffusion in stably-stratified rotating fluids. In Sect. 5, key scaling laws are derived for both the inflectional and inertial instabilities as a function of the stratification and thermal diffusivity. Finally, conclusions and perspectives of this work are presented in Sect. 6.

## 2. Problem formulation

### 2.1. Governing equations and base equilibrium state

We consider the Euler equations under the Boussinesq approximation and the heat transport equation in the Cartesian coordinate  $(x, y, z)$  in a local frame rotating with angular velocity  $\Omega$ :

$$\nabla \cdot \mathbf{u} = 0, \quad (1)$$

$$\frac{\partial \mathbf{u}}{\partial t} + (\mathbf{u} \cdot \nabla) \mathbf{u} + \mathbf{f} \times \mathbf{u} = -\frac{1}{\rho_0} \nabla p - \alpha_T \theta \mathbf{g}, \quad (2)$$

$$\frac{\partial \theta}{\partial t} + \mathbf{u} \cdot \nabla \theta = \kappa_0 \nabla^2 \theta, \quad (3)$$

where  $\mathbf{u} = (u, v, w)$  is the velocity,  $p$  is the pressure,  $\theta = T - T_0$  is the temperature deviation from the reference temperature  $T_0$ ,  $\mathbf{f} = (0, 0, 2\Omega)$  is the Coriolis vector which is here anti-aligned with the gravity  $\mathbf{g} = (0, 0, -g)$ ,  $\rho_0$  is the reference density,  $\kappa_0$  is the reference thermal diffusivity,  $\alpha_T$  is the thermal expansion coefficient, and  $\nabla^2$  denotes the Laplacian operator. We thus consider as a first step the traditional  $f$ -plane case corresponding

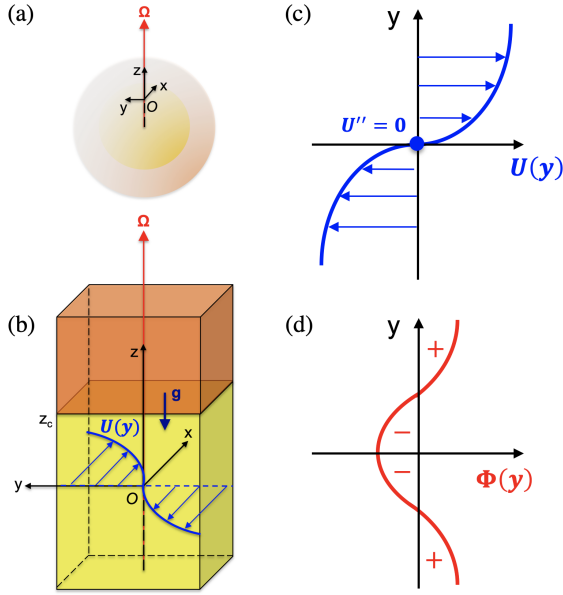


**Fig. 1.** (a,b) Horizontal shear flow  $U(y)$  on a local polar plane rotating with angular speed  $\Omega$  in the radiative zone of a rotating star. The radiative and convective zones, colored as yellow and orange with the transition altitude  $z_c$ , are the configuration of low-mass stars; it should be inverted for early-type stars. (c) Horizontal shear flow profile  $U(y)$  with an inflection point  $U'' = 0$  for the inflectional instability. (d) Rayleigh discriminant  $\Phi(y) = f_0(f_0 - U')$  for the inertial instability configuration.

to the horizontal shear flow on the pole (Fig. 1) to compare with previous literature. In this set-up, the action of the latitudinal component of the rotation vector is filtered out (Gerkema & Shrira 2005; Gerkema et al. 2008). The current Cartesian coordinates  $(x, y, z)$  on the traditional  $f$ -plane is associated with the spherical coordinates  $(r, \theta_s, \varphi)$  where  $r$  is the radial coordinate and  $\varphi$  is the longitude. For instance,  $x$  is the longitudinal coordinate with  $\mathbf{e}_x = \mathbf{e}_\varphi$  where  $\mathbf{e}$  denotes the unit vector of the coordinate systems,  $y$  is the latitudinal coordinate with  $\mathbf{e}_y = -\mathbf{e}_\theta$ , and  $z$  is the vertical coordinate with  $\mathbf{e}_z = \mathbf{e}_r$ .

To perform the linear stability analysis, we consider a steady base velocity  $\mathbf{U} = (U(y), 0, 0)$  in a hyperbolic tangent form

$$U = U_0 \tanh\left(\frac{y}{L_0}\right), \quad (4)$$

where  $U_0$  and  $L_0$  are the reference velocity and length scale, respectively. We consider a base temperature profile  $\bar{\Theta}(z)$  which increases linearly with height  $z$ :

$$\bar{\Theta} = \frac{\Delta\Theta_0}{\Delta z} z, \quad (5)$$

where  $\Delta\Theta_0$  is the base-temperature difference along the vertical distance  $\Delta z$ .

## 2.2. Linearized stability equations

Subject to the base state, we consider perturbations  $\tilde{\mathbf{u}} = \mathbf{u} - \mathbf{U} = (\tilde{u}, \tilde{v}, \tilde{w})$ ,  $\tilde{p} = p - \bar{P}$  where  $\bar{P}$  is the base pressure profile and  $\tilde{T} = \theta - \bar{\Theta}$ . Hereafter, we use dimensionless parameters by converting the equations (1-3) into a set of dimensionless equations with the length scale as  $L_0$ , the velocity scale as  $U_0$ , the time scale as  $L_0/U_0$ , the pressure scale as  $\rho_0 U_0^2$  and the temperature scale as

$(L_0 \Delta\Theta_0)/\Delta z$ . For infinitesimally small-amplitude perturbations, we obtain the following linearized perturbation equations

$$\frac{\partial \tilde{u}}{\partial x} + \frac{\partial \tilde{v}}{\partial y} + \frac{\partial \tilde{w}}{\partial z} = 0, \quad (6)$$

$$\frac{\partial \tilde{u}}{\partial t} + U \frac{\partial \tilde{u}}{\partial x} + (U' - f) \tilde{v} = -\frac{\partial \tilde{p}}{\partial x}, \quad (7)$$

$$\frac{\partial \tilde{v}}{\partial t} + U \frac{\partial \tilde{v}}{\partial x} + f \tilde{u} = -\frac{\partial \tilde{p}}{\partial y}, \quad (8)$$

$$\frac{\partial \tilde{w}}{\partial t} + U \frac{\partial \tilde{w}}{\partial x} = -\frac{\partial \tilde{p}}{\partial z} + N^2 \tilde{T}, \quad (9)$$

$$\frac{\partial \tilde{T}}{\partial t} + U \frac{\partial \tilde{T}}{\partial x} + \tilde{w} = \frac{1}{Pe} \nabla^2 \tilde{T}, \quad (10)$$

where prime denotes the total derivative with respect to  $y$ ,  $N$  is the dimensionless Brunt-Väisälä frequency where

$$N^2 = \frac{\alpha_T g L_0^2}{U_0^2} \frac{\Delta\Theta_0}{\Delta z}, \quad (11)$$

$f$  is the dimensionless Coriolis parameter

$$f = \frac{2\Omega L_0}{U_0} \quad (12)$$

and  $Pe$  is the Péclet number

$$Pe = \frac{U_0 L_0}{\kappa_0}. \quad (13)$$

Note that  $N^2$  is similar to the Richardson number  $Ri$  defined as  $Ri = N_v^2/S_v^2$  where  $S_v$  is the vertical shear and  $N_v$  is the Brunt-Väisälä frequency used for the vertical shear instability study (Lignières et al. 1999). The non-dimensional  $f$  is equal to the inverse of the Rossby number  $Ro = 1/f$ .

To perform a linear stability analysis, we consider a normal mode representation for the perturbation variables:

$$(\tilde{u}, \tilde{p}, \tilde{T}) = \Re \left[ (\hat{u}(y), \hat{p}(y), \hat{T}(y)) \exp[i(k_x x + k_z z) + \sigma t] \right], \quad (14)$$

where  $i^2 = -1$ ,  $\hat{\mathbf{u}} = (\hat{u}, \hat{v}, \hat{w})$ ,  $\hat{p}$  and  $\hat{T}$  are the latitudinal mode shapes for velocity, pressure and temperature perturbation, respectively,  $k_x$  is the horizontal wavenumber in streamwise direction,  $k_z$  is the vertical wavenumber, and  $\sigma = \sigma_r + i\sigma_i$  is the complex growth rate where the real part  $\sigma_r$  is the growth rate and the imaginary part  $\sigma_i$  is the temporal frequency. Applying the normal mode method, we obtain the following linear stability equations

$$ik_x \hat{u} + \frac{\partial \hat{v}}{\partial y} + ik_z \hat{w} = 0, \quad (15)$$

$$(\sigma + ik_x U) \hat{u} + (U' - f) \hat{v} = -ik_x \hat{p}, \quad (16)$$

$$(\sigma + ik_x U) \hat{v} + f \hat{u} = -\hat{p}_y, \quad (17)$$

$$(\sigma + ik_x U) \hat{w} = -ik_z \hat{p} + N^2 \hat{T}, \quad (18)$$

$$(\sigma + ik_x U) \hat{T} + \hat{w} = \frac{1}{Pe} \hat{\nabla}^2 \hat{T}, \quad (19)$$

where  $\hat{\nabla}^2 = d^2/dy^2 - k^2$  with  $k^2 = k_x^2 + k_z^2$ . Due to the symmetry  $\sigma(k_x, k_z) = \sigma(k_x, -k_z) = \sigma(-k_x, k_z)^* = \sigma(-k_x, -k_z)^*$  where the asterisk  $*$  denotes the complex conjugate; we thus consider only the positive wavenumbers  $k_x$  and  $k_z$  in this paper. For convenience and mathematical simplicity, the set of equations (15-19) can be simplified into a single 4th-order ordinary differential equation (ODE) for  $\hat{T}$ :

$$\begin{aligned} & \frac{d^2 \hat{T}}{dy^2} + \left( \frac{4ss'}{s^2 - N^2} - \frac{\Gamma'}{\Gamma} \right) \frac{d\hat{T}}{dy} \\ & + \left[ k_z^2 \frac{\Gamma}{N^2 - s^2} - k_x^2 + f \frac{k_x \Gamma'}{s\Gamma} + \frac{2ss'}{s^2 - N^2} \left( \frac{U''}{U'} + \frac{s'}{s} - \frac{\Gamma'}{\Gamma} \right) \right] \hat{T} \\ & + \frac{1}{Pe} \left( \frac{is}{s^2 - N^2} \right) \left[ \hat{\nabla}^4 \hat{T} + \left( \frac{s'}{s} - \frac{\Gamma'}{\Gamma} \right) \hat{\nabla}^2 \frac{d\hat{T}}{dy} + \right. \\ & \left. \left\{ \frac{s'}{s} \left( \frac{U''}{U'} - \frac{\Gamma'}{\Gamma} \right) + f \left( \frac{k_x \Gamma'}{s\Gamma} - \frac{k_z^2}{s^2} (U' - f) \right) \right\} \hat{\nabla}^2 \hat{T} \right] = 0, \quad (20) \end{aligned}$$

where  $\hat{\nabla}^4 = (\hat{\nabla}^2)^2$ ,  $s = -i\sigma + k_x U$  is the complex Doppler-shifted frequency, and  $\Gamma$  is the function defined as

$$\Gamma = s^2 + f(U' - f). \quad (21)$$

Note that the ODE (20) becomes a second order ODE in the non-diffusive limit  $Pe \rightarrow \infty$  while it becomes independent of  $N$  for the high-diffusivity case as  $Pe \rightarrow 0$ .

### 2.3. Numerical method

We solve the set of equations (15-19) numerically by considering an eigenvalue problem in a simplified matrix form:

$$\mathcal{A} \begin{pmatrix} \hat{u} \\ \hat{v} \\ \hat{\theta} \end{pmatrix} = \sigma \mathcal{B} \begin{pmatrix} \hat{u} \\ \hat{v} \\ \hat{\theta} \end{pmatrix}, \quad (22)$$

where  $\mathcal{A}$  and  $\mathcal{B}$  are operator matrices expressed as

$$\mathcal{A} = \begin{bmatrix} \mathcal{A}_{11} & \mathcal{A}_{12} & 0 \\ ik^2 f & \mathcal{A}_{22} & N^2 k_z \frac{d}{dy} \\ ik_x & \frac{d}{dy} & k_x k_z U + \frac{ik_z}{Pe} \hat{\nabla}^2 \end{bmatrix}, \quad (23)$$

$$\mathcal{B} = \begin{bmatrix} -\frac{d}{dy} & ik_x & 0 \\ 0 & i\hat{\nabla}^2 & 0 \\ 0 & 0 & ik_z \end{bmatrix}, \quad (24)$$

where

$$\begin{aligned} \mathcal{A}_{11} &= ik_x \left( U' + U \frac{d}{dy} \right) - ik_x f, \\ \mathcal{A}_{12} &= k_x^2 U + (U' - f) \frac{d}{dy} + U'', \\ \mathcal{A}_{22} &= k_x U \hat{\nabla}^2 + f k_x \frac{d}{dy} - k_x U''. \end{aligned} \quad (25)$$

The eigenvalue problem (22) is discretized in  $y$ -direction using the rational Chebyshev functions with the mapping  $\tilde{y} = y/\sqrt{1+y^2}$  projecting the Chebyshev domain  $\tilde{y} \in (-1, 1)$  onto the physical space  $y \in (-\infty, \infty)$  (Deloncle et al. 2007; Park 2012). Vanishing boundary conditions are imposed for  $y \rightarrow \pm\infty$  by suppressing terms in the first and last rows of the operator matrices (Antkowiak 2005). The numerical results are validated with those from Deloncle et al. (2007) and Arobone & Sarkar (2012) in stratified and rotating fluids.

### 3. General results

Horizontal shear flows in stably-stratified and rotating fluids are prone to be unstable by two types of instability mechanisms: the inflectional and inertial instabilities. The inflectional instability occurs when there exists an inflection point  $y_i$  where  $U''(y_i) = 0$ . On the other hand, the inertial instability can occur without an inflection point when there is a centrifugal imbalance between the pressure gradient and rotating flows (Kloosterziel & van Heijst 1991). For the hyperbolic-tangent flow (4) in stratified-rotating fluids, the inflectional instability is always present while the inertial instability exists only in the range  $0 < f < 1$  (Arobone & Sarkar 2012).

Within this range, we display contours of the most unstable growth rate with thermal diffusion at  $Pe = 0.1$  to locate the inflectional and inertial instabilities in the parameter space  $(k_x, k_z)$  (Fig. 2a) for  $f = 0.5$  and  $N = 1$ . Frequency  $\sigma_i$  of the most unstable mode is zero thus not plotted as contours in the parameter space  $(k_x, k_z)$ . At  $k_z = 0$ , we can derive a single 2nd-order ODE for  $\hat{v}$  from the continuity equation (15) and momentum equations (16-17):

$$\frac{d^2 \hat{v}}{dy^2} - \left( k_x^2 + \frac{k_x U'''}{s} \right) \hat{v} = 0. \quad (26)$$

It is important to note that the equation (26) does not depend on neither stratification, rotation nor thermal diffusion, so the two-dimensional inflectional instability is consequently found to be independent of  $N$ ,  $f$  and  $Pe$ . Furthermore, we numerically verified that the inflectional instability is most unstable in the two-dimensional case at  $(k_x, k_z) = (0.445, 0)$  for any values of  $N$  and  $Pe$  in the inertially-stable range ( $f \geq 1$  or  $f \leq 0$ ). On the other hand, in the inertially-unstable range  $0 < f < 1$ , the growth rate increases as  $k_z$  increases at  $k_x = 0.445$  due to the inertial instability (Fig. 2a), and the most unstable growth rate of the inertial instability is found as  $k_z \rightarrow \infty$  at  $k_x = 0$ .

Fig. 2(b) shows an example of the growth rate  $\sigma_r$  as a function of  $k_z$  at  $k_x = 0$ . There are not only one unstable branch but countless number of growth-rate branches (but only the first four branches are shown in Fig. 2b for clarity). We see that the first branch is most unstable and all the branches asymptote certain values as  $k_z$  increases. Arobone & Sarkar (2012) argues that the inertial instability growth approaches to  $\sigma_{\max} = \sqrt{f(1-f)}$ . In the next section, the reasons why there are infinite number of branches and why they approach to  $\sqrt{f(1-f)}$  as  $k_z \rightarrow \infty$  will be explained by means of the WKBJ approximation. Fig. 2(c) shows  $\sigma_r$  versus  $k_z$  at  $k_x = 0.445$ . We see that the first branch starts from  $\sigma_r = 0.1897$  at  $k_z = 0$  due to the inflectional instability, while other branches start at  $\sigma_r = 0$  and increase with  $k_z$ . The increase of the growth rate  $\sigma_r$  with  $k_z$  occurs only in the inertially-unstable regime ( $0 < f < 1$ ) since the inflectional instability is stabilized as  $k_z$  increases in the inertially-stable regime (see e.g. dashed line in Fig. 2c for  $f = 0$ ).

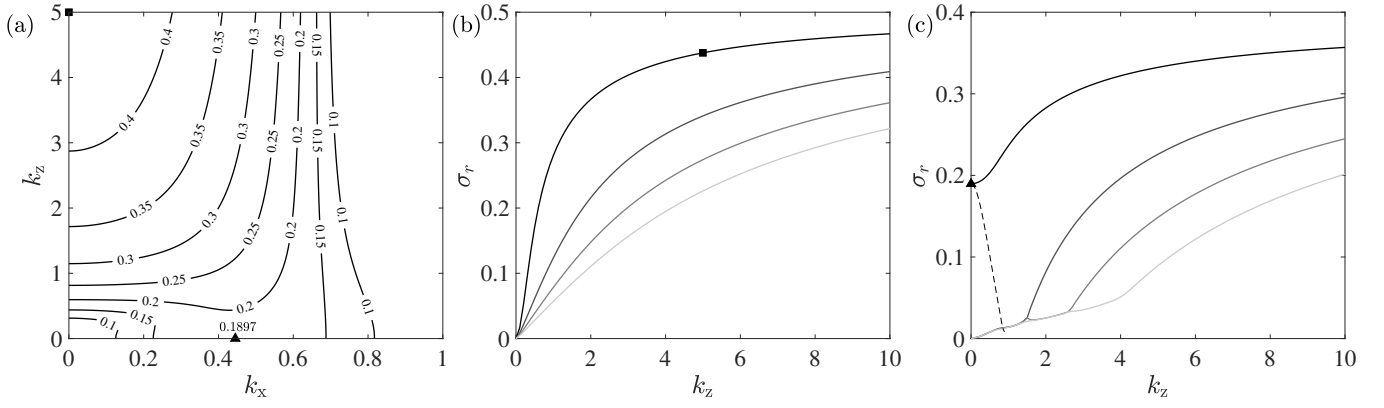


**Fig. 2.** (a) Contours of the maximum growth rate  $\sigma_{\max}$  in the parameter space of  $(k_x, k_z)$  for  $f = 0.5$ ,  $N = 1$ ,  $Pe = 0.1$ . (b,c) Corresponding growth rates  $\sigma_r$  versus vertical wavenumber  $k_z$  at (b)  $k_x = 0$  and (c)  $k_x = 0.445$ . For clarity, only the first four eigenvalue branches are plotted. The dashed line in (c) denotes the growth rate for non-rotating case  $f = 0$ . Symbols denote the parameters for eigenfunctions displayed in Fig. 3.

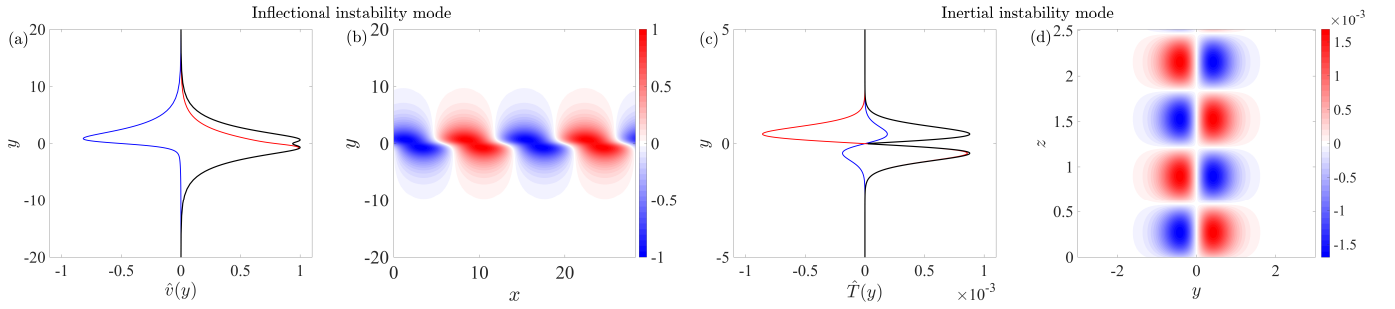


**Fig. 3.** Examples of eigenmodes at (a,b)  $(k_x, k_z) = (0.445, 0)$  for the inflectional instability (triangle in Fig. 2) and (c,d)  $(k_x, k_z) = (0, 5)$  for the inertial instability (square in Fig. 2). (a) and (c) shows the mode shape of  $\hat{v}(y)$  and  $\hat{T}(y)$  (blue: real part, red: imaginary part, black: absolute value), respectively. (b) and (d) shows the perturbations  $\tilde{v}(x, y)$  and  $\tilde{T}(y, z)$  in the physical space, respectively.

Fig. 3 shows examples of modes for the inflectional instability at  $(k_x, k_z) = (0.445, 0)$  (a,b), and the inertial instability at  $(k_x, k_z) = (0, 5)$  (c,d) for the same parameters used in Fig. 2. For both instability modes, the mode shapes are normalized by the maximum of  $|\hat{v}|$ . On the one hand, we represent  $\hat{v}$  for the inflectional instability to be able to compare with the previous literature. On the other hand, we represent  $\hat{T}$  for the inertial instability since this is the quantity we will use for its asymptotic analysis in Sect. 4. For the inflectional instability mode, the mode shape  $\hat{v}$  decreases exponentially as  $y \rightarrow \pm\infty$  while its imaginary part has one zero crossing. If plotted in physical space, we see that the perturbation  $\tilde{v}(x, y)$  is slightly inclined against the direction of the shear. On the other hand, the mode shape  $\hat{T}$  of the inertial instability mode shows there exists a zero crossing for the absolute part of  $\hat{T}$  at  $y = 0$  while decaying exponentially as  $y \rightarrow \pm\infty$ . The temperature perturbation  $\tilde{T}$  in the space  $(y, z)$  shows that the inertial instability mode has an aligned wave pattern with a zero-crossing at  $y = 0$ . One zero-crossing corresponds to the first branch, which is the most unstable branch for given  $k_x$  and  $k_z$ , and higher branches have multiple zero-crossings accordingly.

#### 4. WKBJ analysis for the inertial instability

The maximum growth rate of the inertial instability is proposed as  $\sigma_{\max} = \sqrt{f(1-f)}$  (Arobone & Sarkar 2012). We also verified numerically that the most unstable growth rate is reached as  $k_z \rightarrow \infty$  at  $k_x = 0$ . But it is still not clear why this maximum growth rate  $\sigma_{\max}$  is attained as  $k_z \rightarrow \infty$ , and when the inertial instability occurs in parameter ranges of  $k_z$ ,  $N$ ,  $f$  and  $Pe$ . In this section, we detail mathematical and physical interpreta-

tions of the inertial instability by means of the WKBJ approximation in the limit of large  $k_z$  at  $k_x = 0$ . Similar asymptotic analyses have been performed to understand the instability mechanisms in rotating shear flows (Park & Billant 2012; Park et al. 2017). To understand the effect of thermal diffusion, we perform an asymptotic analysis at two limits:  $Pe \rightarrow \infty$  (i.e. no thermal diffusion) and  $Pe \rightarrow 0$  (i.e. high thermal diffusivity). It is noticeable that the diffusion is often neglected by taking  $Pe \rightarrow \infty$  to understand geophysical flows in the atmosphere and oceans of the Earth (Yavneh et al. 2001; Park et al. 2018), while the high thermal diffusivity case with  $Pe \rightarrow 0$  is studied in astrophysical context for shear instability and mixing in stellar interiors (Lignières et al. 1999; Prat & Lignières 2014). In the following subsections, explicit expressions of asymptotic dispersion relations for the inertial instability in stratified and rotating fluids will be provided in both limits of  $Pe$ .

##### 4.1. The weak diffusion limit: $Pe \rightarrow \infty$

We first consider the 4th-order ODE (20) for  $k_x = 0$ :

$$\begin{aligned} \frac{d^4 \hat{T}}{dy^4} - \frac{\Gamma'}{\Gamma} \frac{d^3 \hat{T}}{dy^3} - \left[ k_z^2 \left( 1 - \frac{\Gamma}{\sigma^2} \right) + Pe \left( \frac{N^2 + \sigma^2}{\sigma} \right) \right] \frac{d^2 \hat{T}}{dy^2} + \\ \left[ k_z^2 \frac{\Gamma'}{\Gamma} + Pe \left( \frac{N^2 + \sigma^2}{\sigma} \right) \frac{\Gamma'}{\Gamma} \right] \frac{d \hat{T}}{dy} - \left[ k_z^4 \frac{\Gamma}{\sigma^2} + k_z^2 Pe \left( \frac{\Gamma}{\sigma} \right) \right] \hat{T} = 0. \end{aligned} \quad (27)$$

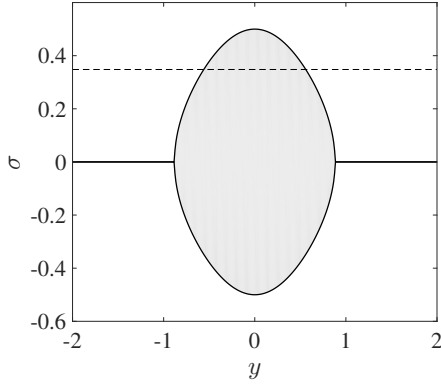


**Fig. 4.** Turning growth rates  $\sigma_{\pm}(y)$  for  $f = 0.5$  (black solid lines) and an example of the growth rate  $\sigma = 0.348$  at  $(k_x, k_z) = (0, 5)$  for  $N = 1$  and  $Pe = \infty$  (dashed line). White and gray areas represent the regions where the solution is exponential and wavelike, respectively.

In the limit  $Pe \rightarrow \infty$ , higher-order derivatives are neglected and we have the following 2nd-order ODE

$$\frac{d^2 \hat{T}}{dy^2} - \frac{\Gamma'}{\Gamma} \frac{d\hat{T}}{dy} + k_z^2 \frac{\Gamma}{N^2 + \sigma^2} \hat{T} = O\left(\frac{1}{Pe}\right). \quad (28)$$

Applying the WKBJ approximation to (28) for large  $k_z$ :

$$\hat{T}(y) \sim \exp\left[\frac{1}{\delta} \sum_{l=0}^{\infty} \delta^l S_l(y)\right], \quad (29)$$

where we have  $\delta = k_z^{-1}$ , we get the following expression of exponential solutions if  $\Gamma < 0$ :

$$\hat{T}(y) = (-\Gamma)^{1/4} \left[ A_1 \exp\left(k_z \int_y \sqrt{\frac{-\Gamma}{\sigma^2 + N^2}} dy\right) + A_2 \exp\left(-k_z \int_y \sqrt{\frac{-\Gamma}{\sigma^2 + N^2}} dy\right) \right], \quad (30)$$

where  $A_1$  and  $A_2$  are constants, or wavelike solutions if  $\Gamma > 0$ :

$$\hat{T}(y) = \Gamma^{1/4} \left[ B_1 \exp\left(ik_z \int_y \sqrt{\frac{\Gamma}{\sigma^2 + N^2}} dy\right) + B_2 \exp\left(-ik_z \int_y \sqrt{\frac{\Gamma}{\sigma^2 + N^2}} dy\right) \right], \quad (31)$$

where  $B_1$  and  $B_2$  are constants. Since  $\sigma^2 + N^2$  is always positive, the sign of  $\Gamma$  determines whether the solutions are evanescent or wavelike. These exponential behaviors depending on  $y$  can be determined by turning points  $y_t$  where  $\Gamma(y_t) = 0$ . It is also convenient to introduce the turning growth rates  $\sigma_{\pm}$ :

$$\sigma_{\pm} = \pm \Re \left[ \sqrt{f(U' - f)} \right], \quad (32)$$

which inform us where  $\Gamma = -\sigma^2 + f(U' - f)$  becomes zero. For instance, if the growth rate is  $\sigma = 0.348$  (i.e. a growth rate obtained numerically for  $f = 0.5$ ,  $N = 1$ ,  $Pe = \infty$ ,  $k_x = 0$ ,  $k_z = 5$ ), there exist two turning points around  $y = \pm 0.560$  (see Fig. 4). Note that  $\sigma_{\pm} = \pm \Re(\sqrt{-\Phi})$  so we can verify where the Rayleigh's discriminant  $\Phi(y) = f(f - U')$  becomes negative.

When the growth rate lies between the two turning growth rates  $\sigma_- < \sigma < \sigma_+$ , this implies that the solutions are wavelike with  $\Gamma > 0$  (gray area in Fig. 4), while the solutions are

evanescent outside this range (white area in Fig. 4). For other values of  $\sigma$ , we can decide whether we can construct eigenfunctions. For example, if  $0 < \sigma < \max(\sigma_+)$  or  $\min(\sigma_-) < \sigma < 0$  like the case  $\sigma = 0.4232 < \max(\sigma_+) = 0.5$  in Fig. 3(c,d), the solution is exponential outside the turning points  $y_{t\pm}$  and wavelike in between. In this case, we can construct an eigenfunction which decays exponentially as  $y \rightarrow \pm\infty$  due to the presence of two turning points. On the other hand, if the growth rate is either  $\sigma > \max(\sigma_+)$  or  $\sigma < \min(\sigma_-)$ , then there is no turning point and solutions are always evanescent for all  $y$ . Therefore, we must impose  $A_1 = A_2 = 0$  to make the solution decaying with  $y \rightarrow \pm\infty$  and no eigenfunction can be constructed in this case. This also implies that, to construct the inertial instability mode, the growth rate does not surpass  $\max(\sigma_+) = \sqrt{f(1-f)}$ .

For an unstable case in the growth-rate range  $0 < \sigma < \max(\sigma_+)$ , we can further derive expressions for the asymptotic dispersion relation by performing a turning point analysis. We first consider the evanescent WKBJ solution that decays exponentially for  $y > y_{t+}$ :

$$\hat{T}(y) = A_{\infty} (-\Gamma)^{1/4} \exp\left(-k_z \int_{y_{t+}}^y \sqrt{\frac{-\Gamma}{\sigma^2 + N^2}} dy\right), \quad (33)$$

where  $A_{\infty}$  is a constant. Around the turning point  $y_{t+}$ , the WKBJ solution (33) is no longer valid and we need to find a local solution that matches with the WKBJ solution in the range  $y_{t-} < y < y_{t+}$ . If we consider a new scaling  $\tilde{y} = (y - y_{t+})/\epsilon$  and an approximation  $\Gamma(y) \sim \Gamma'_{t+} \epsilon \tilde{y}$ , we obtain the following local equation

$$\frac{d^2 \hat{T}}{d\tilde{y}^2} - \frac{1}{\tilde{y}} \frac{d\hat{T}}{d\tilde{y}} - \tilde{y} \hat{T} = O(\epsilon), \quad (34)$$

where  $\epsilon = [k_z^2 (-\Gamma'_{t+}) / (N^2 + \sigma^2)]^{-1/3}$ . Solutions of this local equation (34) can be expressed in terms of derivatives of the Airy functions:  $\hat{T}(\tilde{y}) = a_1 \text{Ai}'(\tilde{y}) + b_1 \text{Bi}'(\tilde{y})$ , where  $a_1$  and  $b_1$  are constants to be matched from the asymptotic behavior of the WKBJ solution (33) as  $y \rightarrow y_{t+}$ . From the asymptotic behaviors of the Airy functions when  $\tilde{y} \rightarrow \pm\infty$ , we obtain the matched WKBJ solution in the region  $y_{t-} < y < y_{t+}$ :

$$\hat{T}(y) = \Gamma^{1/4} \left[ C_+ \exp\left(ik_z \int_{y_{t+}}^y \sqrt{\frac{\Gamma}{\sigma^2 + N^2}} dy\right) + C_- \exp\left(-ik_z \int_{y_{t+}}^y \sqrt{\frac{\Gamma}{\sigma^2 + N^2}} dy\right) \right], \quad (35)$$

where

$$C_+ = \exp\left(-i\frac{\pi}{4}\right) A_{\infty}, \quad C_- = \exp\left(i\frac{\pi}{4}\right) A_{\infty}. \quad (36)$$

Similarly, the solution in  $y < y_{t-}$

$$\hat{T}(y) = A_{-\infty} (-\Gamma)^{1/4} \exp\left(k_z \int_{y_{t-}}^y \sqrt{\frac{-\Gamma}{\sigma^2 + N^2}} dy\right), \quad (37)$$

matches with the following solution in  $y_{t-} < y < y_{t+}$

$$\hat{T}(y) = \Gamma^{1/4} \left[ B_+ \exp\left(ik_z \int_{y_{t-}}^y \sqrt{\frac{\Gamma}{\sigma^2 + N^2}} dy\right) + B_- \exp\left(-ik_z \int_{y_{t-}}^y \sqrt{\frac{\Gamma}{\sigma^2 + N^2}} dy\right) \right], \quad (38)$$

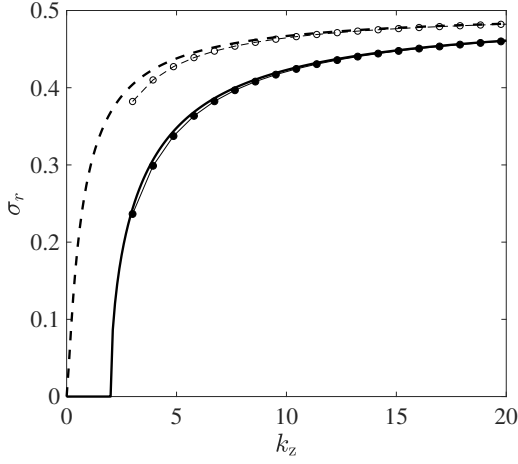


**Fig. 5.** Growth rates of the first branch for  $Pe = \infty$  (solid line) and  $Pe = 0.01$  (dashed line) at  $f = 0.5$  and  $N = 1$  with predictions from the WKBJ dispersion relations (41) for  $Pe = \infty$  (solid with filled circles) and (55) for  $Pe \rightarrow 0$  (dashed with empty circles).

where

$$B_+ = \exp\left(i\frac{\pi}{4}\right)A_{-\infty}, \quad B_- = \exp\left(-i\frac{\pi}{4}\right)A_{-\infty}. \quad (39)$$

Matching the wavelike solutions (35) and (38), we obtain the dispersion relation in the form of a quantization formula:

$$k_z \int_{y_{l-}}^{y_{l+}} \sqrt{\frac{\Gamma}{\sigma^2 + N^2}} dy = \left(m - \frac{1}{2}\right)\pi, \quad (40)$$

where  $m$  is the branch number with a positive integer. This quantized dispersion relation implies that there exist infinite numbers of discrete growth-rate branches for the inertial instability, as verified in numerical results (Fig. 2b,c). Moreover, the integral on the left-hand side of (40) should become zero as  $k_z \rightarrow \infty$  since the right-hand side term is fixed with a finite  $m$ . This implies that the two turning points should approach together as  $k_z$  goes to infinity. Using this property, we can further Taylor-expand the dispersion relation (40) by assuming that the growth rate can be expanded as  $\sigma = \sigma_0 - \sigma_1 k_z^{-p} + O(k_z^{-2p})$  where  $p$  is a positive value. Applying this growth-rate expansion of  $\sigma$ , we find  $p = 1$  and obtain a more explicit dispersion relation for  $\sigma$  for very large  $k_z$ :

$$\sigma = \sigma_0 - \frac{\sigma_1}{k_z} + O\left(\frac{1}{k_z^2}\right), \quad (41)$$

where

$$\sigma_0 = \sqrt{f(1-f)}, \quad \sigma_1 = \frac{\sqrt{f}}{\sigma_0} \left(m - \frac{1}{2}\right) \sqrt{f(1-f) + N^2}. \quad (42)$$

Since  $\sigma_1$  is a positive value, we see that the maximum growth rate  $\sigma_0 = \sigma_{\max} = \sqrt{f(1-f)}$  is achieved at  $k_z \rightarrow \infty$  for any values of  $m$ . The dispersion relation (41) also implies that the inertial instability only exists in the range  $0 < f < 1$  to have a real-positive  $\sigma_0$ . While the maximum growth rate  $\sigma_{\max}$  is independent of  $N$ , the term  $\sigma_1$  depends on the stratification and increases as  $N$  increases; the growth rate thus decreases with  $N$ . We see in Fig. 5 that the asymptotic dispersion relation (41) matches well with the numerical results as  $k_z$  increases.

The asymptotic dispersion relation (41) also gives rich information on the inertial instability in wide ranges of parameters  $f$

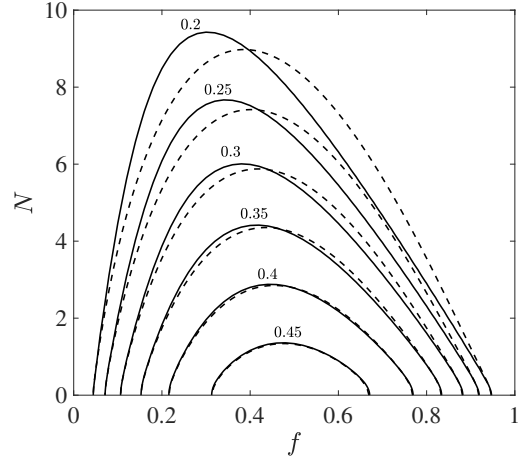


**Fig. 6.** Growth rate contours in the parameter space  $(f, N)$  for  $Pe = \infty$ ,  $k_x = 0$ ,  $k_z = 20$  (solid lines), and predictions from the WKBJ dispersion relation (41) (dashed lines).

and  $N$ . In Fig. 6, we see how the growth rate contours change in the parameter space  $(f, N)$  for  $Pe = \infty$ ,  $k_x = 0$ ,  $k_z = 20$ . At a fixed  $f$ , the growth rate decreases with  $N$ . The contours of the asymptotic growth rate match very well with numerical results especially for higher values of the growth rate. The reason for better agreement for higher growth rate is that the expression (41) is expanded further from (40) based on the assumption that the growth rate is close to its maximum value so that turning points are close to each other.

#### 4.2. The strong diffusion limit: $Pe \rightarrow 0$

Now we investigate the limit  $Pe \rightarrow 0$  for high thermal diffusivity. The 4th-order ODE (27) can be expressed as

$$\frac{d^4 \hat{T}}{dy^4} - \frac{\Gamma'}{\Gamma} \frac{d^3 \hat{T}}{dy^3} - k_z^2 \left(1 - \frac{\Gamma}{\sigma^2}\right) \frac{d^2 \hat{T}}{dy^2} + k_z^2 \frac{\Gamma'}{\Gamma} \frac{d \hat{T}}{dy} - k_z^4 \frac{\Gamma}{\sigma^2} \hat{T} = O(Pe). \quad (43)$$

Applying the WKBJ approximation (29), we obtain the equation at leading order:

$$\frac{1}{\delta^4} S_0'^4 - \frac{k_z^2}{\delta^2} \left(1 - \frac{\Gamma}{\sigma^2}\right) S_0'^2 - k_z^4 \frac{\Gamma}{\sigma^2} = 0, \quad (44)$$

which leads to the solution with  $\delta = k_z^{-1}$ :

$$S_0'^2(y) = -\frac{\Gamma}{\sigma^2}, \quad \text{or} \quad S_0'^2(y) = 1. \quad (45)$$

The general WKBJ solution with  $S_0'^2(y) = 1$  is

$$\hat{T}(y) = D_3 \exp(k_z y) + D_4 \exp(-k_z y), \quad (46)$$

but it has no turning point and the two solutions are always exponentially decaying or increasing as  $y \rightarrow \pm\infty$ . Therefore, we must impose  $D_3 = D_4 = 0$  to construct an eigenfunction. With  $S_0'^2 = -\Gamma/\sigma^2$ , the WKBJ solution is wavelike if  $\Gamma > 0$ :

$$\hat{T}(y) = \frac{\Gamma^{1/4}}{|\sigma^2 + \Gamma|} \left[ D_1 \exp\left(ik_z \int_y \frac{\sqrt{\Gamma}}{\sigma} dy\right) + D_2 \exp\left(-ik_z \int_y \frac{\sqrt{\Gamma}}{\sigma} dy\right) \right], \quad (47)$$

or evanescent if  $\Gamma < 0$ :

$$\hat{T}(y) = \frac{(-\Gamma)^{1/4}}{|\sigma^2 + \Gamma|} \left[ E_1 \exp \left( k_z \int_y \frac{\sqrt{-\Gamma}}{\sigma} dy \right) + E_2 \exp \left( -k_z \int_y \frac{\sqrt{-\Gamma}}{\sigma} dy \right) \right]. \quad (48)$$

These solutions in (47) and (48) now have turning points where  $\Gamma = 0$ , which is the same as in the case without thermal diffusion at  $Pe = \infty$ . Therefore, the turning growth rates  $\sigma_{\pm}(y)$  of the solutions (47-48) are essentially the same as the expression (32), and we can construct an eigenfunction if the growth rate  $\sigma$  lies in the ranges  $\min(\sigma_-) < \sigma < 0$  or  $0 < \sigma < \max(\sigma_+)$ .

For  $Pe \rightarrow 0$ , we can also perform a turning point analysis in order to obtain the asymptotic dispersion relation. We consider the WKB solution that decays exponentially for  $y > y_{t+}$ :

$$\hat{T}(y) = E_{\infty} \frac{(-\Gamma)^{1/4}}{|\sigma^2 + \Gamma|} \exp \left( -k_z \int_{y_{t+}}^y \frac{\sqrt{-\Gamma}}{\sigma} dy \right). \quad (49)$$

Around the turning point  $y_{t+}$ , we apply a new scaled coordinate  $\tilde{y} = (y - y_{t+})/\epsilon$  and obtain the following local equation

$$\epsilon \frac{d^4 \hat{T}}{d\tilde{y}^4} - \epsilon \frac{d^3 \hat{T}}{d\tilde{y}^3} - k_z^2 \epsilon^3 \frac{d^2 \hat{T}}{d\tilde{y}^2} + \frac{k_z^2 \epsilon^3}{\tilde{y}} \frac{d\hat{T}}{d\tilde{y}} + \frac{k_z^4 \epsilon^6 (-\Gamma'_{t+})}{\sigma^2} \hat{T} = 0. \quad (50)$$

Here, we take  $\epsilon = [k_z^2 (-\Gamma'_{t+})/\sigma^2]^{-1/3}$  to balance the equation and the 3rd- and 4th-order derivatives become negligible as of order  $O(\epsilon)$ . The final local equation becomes the same as (34) thus the local solution is the sum of derivatives of the Airy functions. By matching the solution around  $y_{t+}$ , we obtain the WKB solution for  $y_{t-} < y < y_{t+}$

$$\hat{T}(y) = \frac{\Gamma^{1/4}}{|\sigma^2 + \Gamma|} \left[ F_+ \exp \left( ik_z \int_{y_{t+}}^y \frac{\sqrt{\Gamma}}{\sigma} dy \right) + F_- \exp \left( -ik_z \int_{y_{t+}}^y \frac{\sqrt{\Gamma}}{\sigma} dy \right) \right], \quad (51)$$

where

$$F_+ = \exp \left( -i\frac{\pi}{4} \right) E_{\infty}, \quad F_- = \exp \left( i\frac{\pi}{4} \right) E_{\infty}. \quad (52)$$

By matching the solution (51) with the solution for  $y < y_{t-}$ :

$$\hat{T}(y) = E_{-\infty} \frac{(-\Gamma)^{1/4}}{|\sigma^2 + \Gamma|} \exp \left( k_z \int_{y_{t-}}^y \frac{\sqrt{-\Gamma}}{\sigma} dy \right), \quad (53)$$

we obtain the following dispersion relation in a quantization form

$$k_z \int_{y_{t-}}^{y_{t+}} \frac{\sqrt{\Gamma}}{\sigma} dy = \left( m_0 - \frac{1}{2} \right) \pi, \quad (54)$$

where  $m_0$  is the positive integer indicating the branch number. Similarly to the previous section, we Taylor-expand the growth rate  $\sigma$  and we obtain an explicit asymptotic dispersion relation for  $\sigma$  as a function of  $k_z$ :

$$\sigma = \sigma_{0,0} - \frac{\sigma_{1,0}}{k_z} + O \left( \frac{1}{k_z^2} \right), \quad (55)$$

where

$$\sigma_{0,0} = \sqrt{f(1-f)}, \quad \sigma_{1,0} = \left( m_0 - \frac{1}{2} \right) \sqrt{f}. \quad (56)$$

We see in Fig. 5 that a numerical result at small  $Pe = 0.01$  matches very well with the asymptotic growth rate (55) in the limit  $Pe \rightarrow 0$  as  $k_z$  increases. It is important to note that the expression of the maximum growth rate is the same as (41) in non-diffusive fluids, and the inertial instability in stratified-rotating fluids with high thermal diffusivity also occurs in the regime  $0 < f < 1$ . In contrast to the non-diffusive case, the term  $\sigma_{1,0}$  is independent of the stratification  $N$ .

### 4.3. Comparison of the growth rates

It is noteworthy that the asymptotic dispersion relation (55) in fluids with high thermal diffusivity is independent of the stratification, and the expression (41) without thermal diffusion becomes identical to (55) as  $N \rightarrow 0$ . This implies that high thermal diffusivity suppresses the effect of the stable stratification. Thus, stratified fluids with high thermal diffusivity behave like unstratified fluids. The term  $\sigma_{1,0}$  at the first order is always smaller than  $\sigma_1$  in (42); therefore, the ratio  $\gamma_1$  between the two terms at first order is always larger than unity for positive  $N$  if we consider the same branch  $m = m_0$ :

$$\gamma_1 = \frac{\sigma_1}{\sigma_{1,0}} = \sqrt{\frac{f(1-f) + N^2}{f(1-f)}} > 1. \quad (57)$$

The growth rate of inertial instability in thermally-diffusive fluids is therefore always larger than that in non-diffusive fluids. The effect of high thermal diffusivity has already been reported in previous literatures for the vertical shear instability (Lignières 1999; Prat & Lignières 2013) but the above expression shows explicitly and quantitatively how much the inertial instability is destabilized by the high thermal diffusivity as shown in Fig. 5.

## 5. Parametric study

### 5.1. Effects of $Pe$ on the inflectional instability

While the inertial instability is accessible by the WKB approximation, the inflectional instability should be investigated numerically since it occurs at low  $k_x$  and  $k_z$ . In Fig. 7(a), we see the growth rate  $\sigma_r$  of the inflectional instability as a function of  $k_z$  for different values of the Péclet number  $Pe$  at  $k_x = 0.445$ ,  $N = 2$  and  $f = 0$ , the regime where only the inflectional instability exists. The growth rate  $\sigma_r$  decreases with  $k_z$  for any values of  $Pe$ , and the stabilization occurs faster as  $Pe$  decreases to zero (i.e. as the thermal diffusivity increases). We see that growth-rate curves (solid lines) approach to the growth-rate curve for the unstratified case at  $N = 0$  (dashed line) as  $Pe$  goes to zero. This implies that high thermal diffusivity suppresses the effect of stratification on the inflectional instability. The suppression of the inflectional instability by the thermal diffusion is also found in fast rotating regime at  $N/f = 0.1$  (Fig. 7b). We see that the instability is sustained at smaller  $k_z$  for the fast rotation with small  $N/f$ , and the stabilization with  $k_z$  is faster as thermal diffusivity increases.

In Fig. 8, we investigate effects of both  $Pe$  and  $N$  on the inflectional instability in the inertially-stable regime at  $f = 0$ . We see in Fig. 8(a) that the growth rate increases as the stratification becomes strong while small  $Pe$  (i.e. strong thermal diffusion) suppresses the instability. For strong stratification  $N \geq 10$ , it is also observed that the shape of growth-rate curves is similar and they just have different onsets of stabilization at lower Péclet numbers (thus higher diffusivity) as  $N$  increases. Due to this resemblance of growth-rate curves for strong stratification, we plot again the growth rate curves versus the rescaled parameter  $PeN^2$



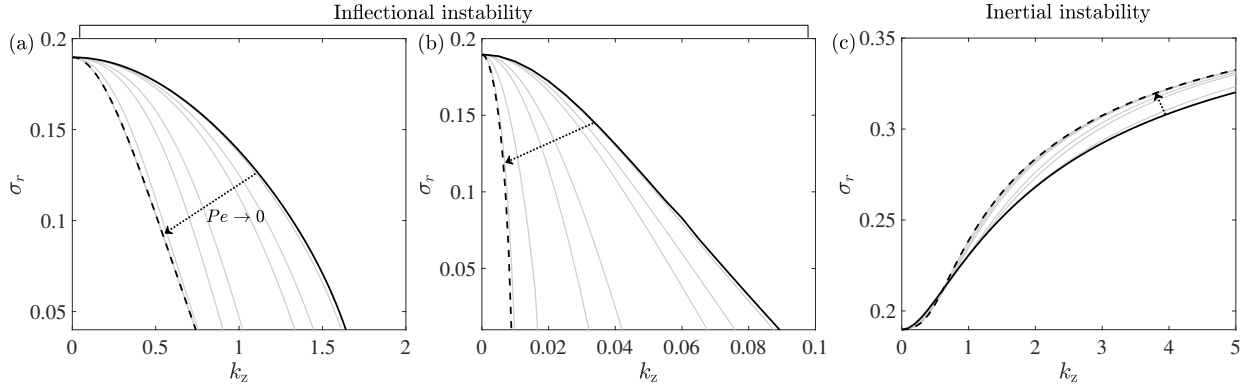


**Fig. 7.** Growth rate  $\sigma_r$  versus vertical wavenumber  $k_z$  at  $k_x = 0.445$  for different Péclet numbers  $Pe$ :  $Pe = \infty$  (black solid line),  $Pe = \{100, 10, 5, 1, 0.5, 0.1, 0.01\}$  (gray solid lines) and other parameters: (a)  $N = 2$ ,  $N/f = \infty$ , (b)  $N = 2$ ,  $N/f = 0.1$ , (c)  $N = 0.5$ ,  $N/f = 1$ . Dashed lines denote the growth rate for unstratified case  $N = 0$ . Arrows indicate the direction of decreasing  $Pe$ .

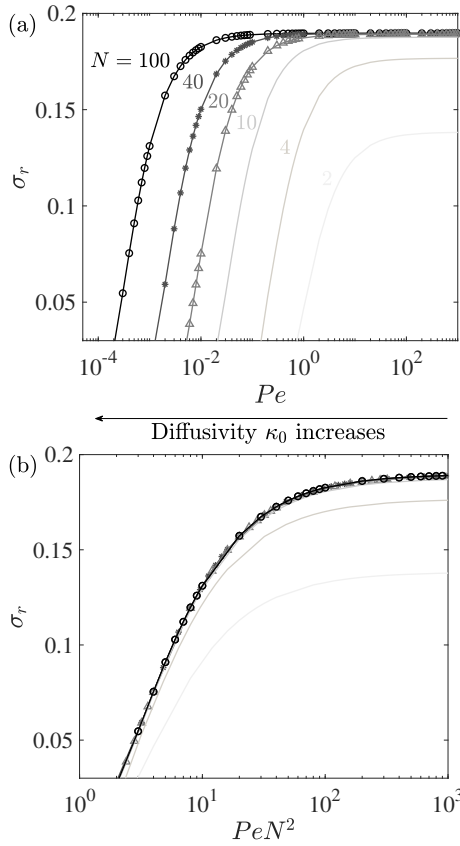


**Fig. 8.** Growth rate of the inflectional instability versus (a)  $Pe$  and (b)  $PeN^2$  for different values of  $N$  at  $k_x = 0.445$ ,  $k_z = 1$  and  $f = 0$ .

in Fig. 8(b). We clearly see that the rescaled growth rate curves collapse well for high  $N$ . This self-similarity represented by the rescaled parameter  $PeN^2$  is reminiscent of the Richardson-Péclet number  $RiPe$  in the small-Péclet-number approximation used for vertically sheared flows in stratified and thermally-diffusive fluids (Lignières 1999; Prat & Lignières 2013).

## 5.2. Effects of $Pe$ on the inertial instability

The WKBJ approximation providing explicit dispersion relations explains that the inertial instability in stratified fluids as  $Pe \rightarrow 0$  becomes equivalent to that in unstratified fluids. Nonetheless, it is imperative to investigate whether this argu-

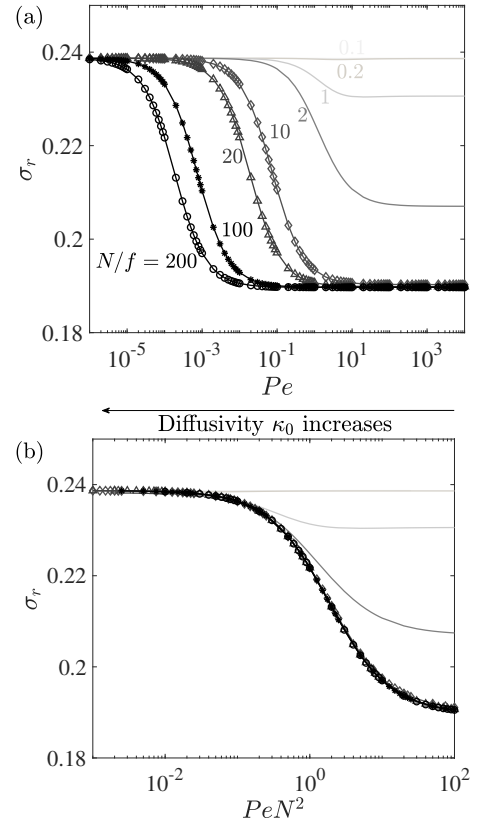


**Fig. 9.** Inertial instability growth rate versus (a)  $Pe$  and (b)  $PeN^2$  for different values of  $N/f$  at  $k_x = 0.445$ ,  $k_z = 1$  and  $f = 0.5$ .

ment is valid for any  $k_x$  and finite  $Pe$  since the WKBJ analysis in this paper is only applied for  $k_x = 0$  in the two extreme limits of  $Pe$ :  $Pe \rightarrow \infty$  and  $Pe \rightarrow 0$ . In the inertially-unstable regime  $f = 0.5$  where both the inflectional and inertial instabilities exist (Fig. 7c), we see that the growth rate in the range  $k_z > 0.6$  is increased while the growth rate in the range  $k_z < 0.6$  is decreased as  $Pe$  decreases to zero. For both cases, we clearly see that the growth-rate curves in diffusive fluids (solid lines) asymptote to the curve for unstratified case at  $N = 0$  (dashed line) as  $Pe \rightarrow 0$ . We can verify from this asymptotic behavior as  $Pe \rightarrow 0$  that the growth rate at small wavenumber  $k_z < 0.6$  corresponds to the inflectional instability while the growth rate at large wavenumber  $k_z > 0.6$  corresponds to the inertial instability.

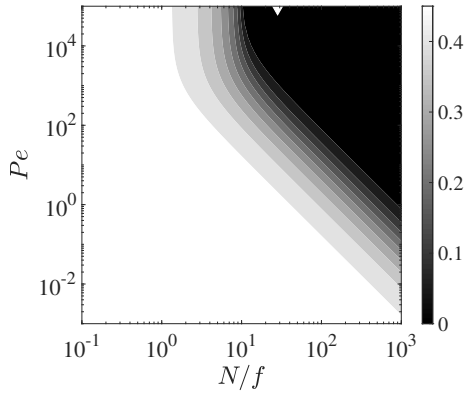


**Fig. 10.** Growth rate contours in the parameter space  $(N/f, Pe)$  for  $f = 0.5$ ,  $k_x = 0$ ,  $k_z = 20$ . The white triangle on the axis denotes the critical  $N/f$  from (58) as  $Pe \rightarrow \infty$ .

Picking up the growth rate of the inertial instability at  $(k_x, k_z) = (0.445, 1)$ , we show in Fig. 9 effects of the Péclet number  $Pe$  on the inertial instability for different values of the ratio  $N/f$  at  $f = 0.5$ . For weakly stratified case with low ratio  $N/f < 1$ , the growth rate remains constant as  $\sigma_r \approx 0.239$  in wide range of  $Pe$ . On the other hand, the growth rate decreases as  $Pe$  increases and asymptotes to  $\sigma_r \approx 0.190$  for high  $N/f$ . Similar to Fig. 8(a), the shape of growth-rate curves for high ratio  $N/f > 10$  resemble with different onsets of stabilization as  $Pe$  increases. As the rescaled parameter  $PeN^2$  is applied for growth rate curves (Fig. 9b), we see that growth-rate curves of the inertial instability for large values of  $N/f$  collapse onto a curve, similar as in the purely inflectional instability case ( $f = 0$ ).

Fig. 10 shows contours of the growth rate  $\sigma_r$  in the parameter space  $(N/f, Pe)$  at  $k_x = 0$ ,  $k_z = 20$ ,  $f = 0.5$ , a typical parameter set for the inertial instability. We see that for a fixed  $N/f$ , the inertial instability destabilizes as the thermal diffusivity increases (i.e. as  $Pe \rightarrow 0$ ), similarly to what is observed in Fig. 9. For a fixed  $Pe$ , the growth rate decreases as  $N/f$  increases. At a fixed rotation, the stratification thus stabilizes the flow. This can be predicted from the case for non-diffusive fluids as  $Pe \rightarrow \infty$  by the asymptotic dispersion relation (41) as the term  $\sigma_1$  increases with  $N$  (i.e. the growth rate decreases with  $N$ ). We can further derive from (41) the critical value of the ratio  $N/f$  in the limit  $Pe \rightarrow \infty$  where the growth rate  $\sigma$  becomes zero:

$$\left. \frac{N}{f} \right|_{\text{crit}} = \sqrt{\frac{(1-f)^2 k_z^2}{(m-1/2)^2 f} - \left( \frac{1-f}{f} \right)}. \quad (58)$$

It is notable that for a fixed  $f$ , the critical ratio  $N/f$  increases with the vertical wavenumber  $k_z$ . This implies that the characteristic vertical length scale  $\lambda_z = 2\pi/k_z$  decreases as the ratio  $N/f$  increases. We see in Fig. 10 that the asymptotic prediction (58) for the critical value of  $N/f$  lies in the stable regime obtained from numerical results.

## 6. Conclusion

This paper investigates instabilities of a horizontal shear flow in stably-stratified, rotating, and thermally-diffusive fluids corresponding to stellar radiative regions. On the one hand, the inflectional shear instability always exists for the horizontal shear flow in a hyperbolic tangent profile and the most unstable growth rate  $\sigma_{\max} = 0.1897$  is attained at  $k_x = 0.445$  and  $k_z = 0$  independently of the stratification, rotation and thermal diffusion. For

this instability, the stable stratification has a destabilising action, which is inhibited by thermal diffusion. This is the opposite of the case of the vertical shear instability, which is inhibited by the stable stratification but favoured by thermal diffusion that again diminishes its effects (e.g. Zahn 1983, 1992). On the other hand, the inertial instability is present in the range of  $0 < f < 1$  and its maximum growth rate  $\sigma_{\max} = \sqrt{f(1-f)}$  is reached as  $k_z \rightarrow \infty$  in the inviscid limit for both non-diffusive and high-diffusivity fluids. The analysis on the inertial instability for the case  $k_x = 0$  and large  $k_z$  has been elaborated further by means of the WKBJ approximation in two limits:  $Pe \rightarrow \infty$  and  $Pe \rightarrow 0$  (i.e. for low and high thermal diffusivity, respectively), and explicit expressions for asymptotic dispersion relations are provided in both limits. For  $Pe \rightarrow \infty$ , the growth rate decreases with  $N$ , the stratification thus stabilizing the inertial instability, but the maximum growth rate  $\sigma_{\max}$  at infinite  $k_z$  remains as  $\sqrt{f(1-f)}$  independent of  $N$ . In the limit  $Pe \rightarrow 0$ , the growth rate is no longer dependent on the stratification and becomes identical to inertial instability growth for the unstratified case at  $N = 0$ . Detailed numerical studies confirm in the general parameter space  $(k_x, k_z)$  that both the inflectional and inertial instabilities in thermally-diffusive fluids asymptote to those of the unstratified case as the thermal diffusivity increases (i.e.  $Pe \rightarrow 0$ ). A self-similarity of the growth rate in stratified-rotating fluids is also found such that the instabilities depend on the parameter  $PeN^2$  for small  $Pe$  and strong stratification  $N$ . As a summary, we describe in Table 1 the growth rate and its variation with parameters  $Pe$ ,  $N$ ,  $f$ ,  $k_x$  and  $k_z$ .

The present work brings to light two horizontal shear instabilities that probably occur in stellar radiative zones but had not been considered in stellar astrophysics before in the case of the inertial instability. The particularity of the stellar regime is that the high thermal diffusivity is able to weaken the stabilizing effect of the stratification for the inertial instability thus to enhance its development, while the inflectional instability is suppressed by the high thermal diffusivity. We first investigated the linear instabilities in the polar regions but their nonlinear saturation and the resulting anisotropic turbulent transport of angular momentum and chemicals in both the horizontal and vertical directions has to be quantified. To derive the associated prescriptions for stellar evolution models, it is therefore necessary to study the effects of the complete Coriolis acceleration on the instabilities at any co-latitude using the so-called non-traditional  $f$ -plane approximation (Gerkema et al. 2008). This will be done in the next article of the series.

**Acknowledgements.** The authors acknowledge support from the European Research Council through ERC grant SPIRE 647383 and from GOLF and PLATO CNES grants at the Department of Astrophysics of CEA.

## References

- Aerts, C., Mathis, S., & Rogers, T. 2019, ARA&A, 57 [arXiv:1809.07779], in press
- Aerts, C., Van Reeth, T., & Tkachenko, A. 2017, ApJ, 847, L7
- Antkowiak, A. 2005, PhD thesis, Université Paul Sabatier de Toulouse
- Arobone, E. & Sarkar, S. 2012, J. Fluid Mech., 703, 29–48
- Billant, P. & Chomaz, J.-M. 2001, Physics of Fluids, 13, 1645
- Cantiello, M., Mankovich, C., Bildsten, L., Christensen-Dalsgaard, J., & Paxton, B. 2014, ApJ, 788, 93
- Ceillier, T., Eggenberger, P., García, R. A., & Mathis, S. 2013, A&A, 555, A54
- Davidson, P. A. 2013, Turbulence in rotating, stratified, and electrically conducting fluids (Cambridge University Press)
- Deheuvels, S., Doğan, G., Goupil, M. J., et al. 2014, A&A, 564, A27
- Deheuvels, S., García, R. A., Chaplin, W. J., et al. 2012, ApJ, 756, 19
- Deloncle, A., Chomaz, J.-M., & Billant, P. 2007, J. Fluid Mech., 570, 297–305
- Eggenberger, P., Buldgen, G., & Salmon, S. J. A. J. 2019, A&A, 626, L1
- Eggenberger, P., Montalbán, J., & Miglio, A. 2012, A&A, 544, L4

**Table 1.** A summary table for the growth rate and its variation with parameters  $Pe$ ,  $N$ ,  $f$ , and  $(k_x, k_z)$  for the inflectional and inertial instabilities.

Instability type	$Pe \downarrow (\kappa_0 \uparrow)$	$N \uparrow$	Values of $\max(\sigma_r)$	Corresponding wavenumbers $(k_x, k_z)$
Inflectional	$\downarrow$	$\uparrow$	0.1897 (independent of $f$ )	(0.445, 0)
Inertial	$\uparrow$	$\downarrow$	$\sqrt{f(1-f)}$ (maximum at $f = 0.5$ )	(0, $\infty$ )

- Fuller, J., Piro, A. L., & Jermyn, A. S. 2019, MNRAS, 485, 3661  
Gagnier, D. & Garaud, P. 2018, ApJ, 862, 36  
Garaud, P., Gagnier, D., & Verhoeven, J. 2017, ApJ, 837, 133  
García, R. A., Turck-Chièze, S., Jiménez-Reyes, S. J., et al. 2007, Science, 316, 1591  
Gehan, C., Mosser, B., Michel, E., Samadi, R., & Kallinger, T. 2018, A&A, 616, A24  
Gerkema, T. & Shrira, V. I. 2005, J. Fluid Mech., 529, 195  
Gerkema, T., Zimmerman, J. T. F., Maas, L. R. M., & van Haren, H. 2008, Rev. Geophys., 46, RG2004  
Kloosterziel, R. C. & van Heijst, G. J. F. 1991, J. Fluid Mech., 223, 1  
Kulenthirarajah, L. & Garaud, P. 2018, ApJ, 864, 107  
Kundu, P. K. & Cohen, I. M. 2001, Fluid Mechanics (Elsevier)  
Kurtz, D. W., Saio, H., Takata, M., et al. 2014, MNRAS, 444, 102  
Lignières, F. 1999, A&A, 348, 933  
Lignières, F., Califano, F., & Mangeney, A. 1999, A&A, 349, 1027  
Maeder, A. 1995, A&A, 299, 84  
Maeder, A. 1997, A&A, 321, 134  
Maeder, A. 2003, A&A, 399, 263  
Maeder, A. 2009, Physics, Formation and Evolution of Rotating Stars (Springer Berlin Heidelberg)  
Maeder, A. & Meynet, G. 1996, A&A, 313, 140  
Maeder, A. & Zahn, J.-P. 1998, A&A, 334, 1000  
Marques, J. P., Goupil, M. J., Lebreton, Y., et al. 2013, A&A, 549, A74  
Mathis, S. 2013, Lecture Notes in Physics, Vol. 865, Transport Processes in Stellar Interiors, ed. M. Goupil, K. Belkacem, C. Neiner, F. Lignières, & J. J. Green (Springer-Verlag Berlin Heidelberg), 23  
Mathis, S., Palacios, A., & Zahn, J.-P. 2004, A&A, 425, 243  
Mathis, S., Prat, V., Amard, L., et al. 2018, A&A, 620, A22  
Mathis, S. & Zahn, J.-P. 2004, A&A, 425, 229  
Meynet, G. & Maeder, A. 2000, A&A, 361, 101  
Michalke, A. 1964, J. Fluid Mech., 19, 543–556  
Mosser, B., Goupil, M. J., Belkacem, K., et al. 2012, A&A, 548, A10  
Murphy, S. J., Fossati, L., Bedding, T. R., et al. 2016, MNRAS, 459, 1201  
Ouazzani, R. M., Marques, J. P., Goupil, M. J., et al. 2019, A&A, 626, A121  
Palacios, A., Charbonnel, C., Talon, S., & Siess, L. 2006, A&A, 453, 261  
Park, J. 2012, PhD thesis, Ecole Polytechnique  
Park, J. & Billant, P. 2012, J. Fluid Mech., 707, 381–392  
Park, J., Billant, P., & Baik, J.-J. 2017, J. Fluid Mech., 822, 80–108  
Park, J., Billant, P., Baik, J.-J., & Seo, J. M. 2018, J. Fluid Mech., 840, 5–24  
Pinçon, C., Belkacem, K., Goupil, M. J., & Marques, J. P. 2017, A&A, 605, A31  
Prat, V., Guilet, J., Viallet, M., & Müller, E. 2016, A&A, 592, A59  
Prat, V. & Lignières, F. 2013, A&A, 551, L3  
Prat, V. & Lignières, F. 2014, A&A, 566, A110  
Richard, D. & Zahn, J.-P. 1999, A&A, 347, 734  
Saio, H., Kurtz, D. W., Takata, M., et al. 2015, MNRAS, 447, 3264  
Schmid, P. & Henningson, D. S. 2001, Stability and Transition in Shear Flows (Springer-Verlag, New York)  
Spada, F., Gellert, M., Arlt, R., & Deheuvels, S. 2016, A&A, 589, A23  
Spruit, H. C. 1999, A&A, 349, 189  
Talon, S. & Charbonnel, C. 2005, A&A, 440, 981  
Talon, S. & Zahn, J.-P. 1997, A&A, 317, 749  
Talon, S., Zahn, J. P., Maeder, A., & Meynet, G. 1997, A&A, 322, 209  
Townsend, A. A. 1958, Journal of Fluid Mechanics, 4, 361  
Van Reeth, T., Mombarg, J. S. G., Mathis, S., et al. 2018, A&A, 618, A24  
Van Reeth, T., Tkachenko, A., & Aerts, C. 2016, A&A, 593, A120  
Yavneh, I., McWilliams, J. C., & Molemaker, M. J. 2001, J. Fluid Mech., 448, 1–21  
Zahn, J.-P. 1983, in Saas-Fee Advanced Course 13: Astrophysical Processes in Upper Main Sequence Stars, ed. A. N. Cox, S. Vauclair, & J. P. Zahn, 253  
Zahn, J.-P. 1992, A&A, 265, 115  
Zahn, J.-P., Talon, S., & Matias, J. 1997, A&A, 322, 320